Using a mixed ionic electronic conductor to build an analog memristive device with neuromorphic programming capabilities

Klaasjan Maas, Edouard Villepreux, David Cooper, Carmen Jimenez, Hervé Roussel, Laetitia Rapenne, Xavier Mescot, Quentin Rafhay, Michel Boudard, Mónica Burriel

Journal of
Materials Chemistry C

Materials for optical, magnetic and electronic devices

Accepted Manuscript

This article can be cited before page numbers have been issued, to do this please use: K. Maas, E. Villepreux, D. Cooper, C. Jiménez, H. Roussel, L. Rapenne, X. Mescot, Q. Rafhay, M. Boudard and M. Burriel, *J. Mater. Chem. C*, 2019, DOI: 10.1039/C9TC03972D.

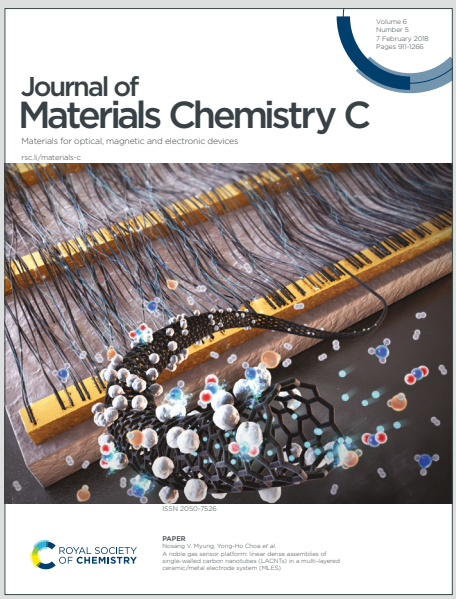

ROYAL SOCIETY OF CHEMISTRY

rsc.li/materials-c

Journal of Materials Chemistry C
View Article Online
DOI: 10.1039/C9TC03972D

Article type: Communication

Using a mixed ionic electronic conductor to build an analog memristive device with neuromorphic programming capabilities

Klaasjan Maas, Edouard Villepreux, David Cooper, Carmen Jimenez, Hervé Roussel, Laetitia Rapenne, Xavier Mescot, Quentin Rafhay, Michel Boudard, Mónica Burriel*

Dr. K. Maas, Dr. C. Jimenez, Dr. H. Roussel, Dr. L. Rapenne, Dr. M. Boudard, Dr. M. Burriel,
Univ. Grenoble Alpes, CNRS, Grenoble INP†, LMGP, F-38000 Grenoble, France
†*Institute of Engineering Univ. Grenoble Alpes*
E-mail: monica.burriel@grenoble-inp.fr
Dr. Q. Rafhay, Dr. X. Mescot
Univ. Grenoble Alpes, CNRS, IMEP-LAHC, F-38000 Grenoble, France
E. Villepreux, Dr. D. Cooper
CEA, LETI, Minatec Campus, F-38054 Grenoble, France

Keywords: Memristive devices, valence change memories, La_2NiO_4, analog switching, neuromorphic

Abstract: Interface-type oxide-based valence-change memories (VCMs) with analog switching capabilities and memory transience are interesting candidates to be used as artificial synapses for the hardware implementation of artificial neural networks (ANN) with short-term synaptic dynamics. Here, the mixed ionic-electronic conducting (MIEC) oxide $La_2NiO_{4+\delta}$ is used to rationally design a new volatile interface-type valence-change memory based on a tunable p-n junction between the p-type MIEC oxide and an n-type "oxygen-reservoir" oxide. The memory does not require a forming step to trigger memristance and exhibits a highly multilevel and bipolar analog-type change in resistance, which can be continuously varied by over two orders of magnitude A distinctive two-step memory transience where the resistance of the unbiased device increases before relaxing back to a lower resistance state was measured and has been attributed to the Fick diffusion of oxygen ions, restoring the drift-induced concentration gradients at the Ti/L2NO4 interface.

Journal of Materials Chemistry C
View Article Online
DOI: 10.1039/C9TC03972D

Artificial neural networks (ANN) are brain-inspired computational architectures where nodes (called neurons) carry out sums of weighted inputs and send signals between each other through adaptable weighted interconnections called synapses.[1] These architectures have recently generated considerable research interest as they are inherently fault tolerant due to their interconnectivity and adaptability, resulting in a highly parallelized computational network, which is beneficial for artificial intelligence tasks and learning processes.[2,3] Adaptive computational systems are capable of self-adjusting their internal state (in this case the synaptic weights) during operation, making the system more efficient as it learns. Although the ANNs currently being used for machine-learning applications and artificial intelligence (AI) are generally composed of a software layer running on CMOS-based von Neumann architectures, there is a strong incentive to investigate the possibilities for their hardware implementation.[4,5] This alternative is fueled by the recent advances in new memristive materials and device architectures for memory applications,[6–10] and in particular in oxide-based valence-change memories (VCMs).[11,12]

Memory volatility is a key feature for emulating short-term synaptic dynamics,[10,13,14] a highly desirable feature for learning applications, as a built-in memory transience (tendency to forget) reduces data over-fitting and allows for a better generalization.[15] By forgetting statistically insignificant details, pattern recognition of artificial deep neural networks is improved in unstructured datasets, preventing them from learning the entire dataset "by heart" which effectively decreases their performance when faced with new unknown data. A transient memory allows synaptic interconnections to decay when unused or exposed to noisy inputs, allowing other connections to strengthen and take over, which helps optimize the neural network and quickly converge to local minima in its efficiency and accuracy during data processing. Recently silver nanoparticles-based memristors with intrinsic volatility (relaxation behavior) were reported to show biorealistic temporal

Journal of Materials Chemistry C
View Article Online
DOI: 10.1039/C9TC03972D

dynamics, a faithful emulation of synaptic plasticity.[16] Remarkably, by integrating these diffusive memristors, which act as artificial neurons, with non-volatile memristive synapses, fully memristive ANNs were created in which unsupervised synaptic weight updating and pattern classification was demonstrated.[6]

In VCMs, the field induced migration of oxygen ions used to program the memory can lead both to a change in the oxygen stoichiometry and the electronic properties (*e.g.* change in carrier concentration) at a given location through redox reactions. VCMs are inherently bipolar memories, as the polarity of the voltage pulse determines whether an oxidation or a reduction reaction takes place, increasing or decreasing the resistance state of the device. The resistance change can take place in a small localized region in case of filamentary-type switching or over the entire metal/oxide interface in case of interfacial switching, although intermediate cases have also been reported.[17] Filamentary-type VCM memories typically show an abrupt transition between two well defined memory states, usually referred-to as the Low Resistance State (LRS) and the High Resistance State (HRS). However, the possibility of showing an abrupt reset (transition from LRS to HRS) and a gradual reset has also been reported in several filamentary systems.[18–21] A gradual reset process is usually easier to achieve as it can be intrinsically considered to be "self-limiting". Indeed, when disconnecting the filament the current drops and Joule heating effects become less and less important. Furthermore, by increasing the gap between the electrode and the filament, the electrical field also decreases, reducing ionic drift and leading to a gradual and ultimately saturating reset process.[20] Filamentary-based resistive switching has certain limitations, such as the need for a forming step and limited multilevel capabilities. A gradual set (transition from HRS to LRS) has been reported in some cases for filamentary systems but requires the use of an additional variable current compliance to define and stabilize each intermediate resistance state.[19] On top of being a hassle for technological

Journal of Materials Chemistry C
View Article Online
DOI: 10.1039/C9TC03972D

implementation, an electroformed device is also subject to highly variable electrical properties.[22,23] Furthermore, the use of a variable current compliance to achieve multilevel memory cells (MLC) also requires additional circuitry, which complicates the chip design. Therefore, to enhance the control over the change in resistance and reliably achieve multilevel memory programming capabilities it is of great interest to build interface-type VCMs, in which the change in resistance can only be achieved in the presence of homogeneous, self-limiting switching mechanisms. Memristive systems that can achieve a gradual change in resistance in both polarities are better candidates to emulate brain functions than their binary counterparts.[24] While insulating materials are prone to result in filamentary switching, initially conducting (or semiconducting) oxides are favorable for interfacial mechanisms.[26] When a highly insulating switching medium is used, the metal/insulator contact resistance is usually negligible, the voltage drop occurs mainly across the insulator, increasing the likelihood of a (soft) dielectric breakdown of the material, generating the active filamentary pathways. Conversely, the contact resistance can become the main contributor to the total resistance of the device when a (semi)conducting material is used as switching medium. The fact that the electric field is mainly concentrated in this interfacial region of the device increases the chances of obtaining interface-type switching.

In the last years Mixed Ionic-Electronic Conducting (MIEC) oxides have emerged as the most effective switching materials to construct area-dependent (interface or volume type) and forming-free valence change memristive devices. Most of the works reporting this type of memristance have focused on the study of manganites, in particular $La_{1-x}Sr_xMnO_{3-\delta}$ (LSM)[27,28], $Pr_{1-x}Ca_xMnO_{3-\delta}$ (PCMO)[29–33] and PCMO/$La_{0.6}Pr_{0.4}MnO_3$ (LPMO) double-layered structures,[34] successfully demonstrating the existence of two non-volatile resistance states. What is more, gradual set and reset, analog neuromorphic synapse functions, in addition to the hardware implementation of the synaptic

Journal of Materials Chemistry C
View Article Online
DOI: 10.1039/C9TC03972D

devices has been successfully demonstrated for PCMO-based hetero-oxide structures.[35–38] The switching is often claimed to be due to the change in contact resistance resulting from the drift of oxygen ions (vacancies) towards and away from an active interface. As a result and depending on the heterostructure the oxygen anions can be trapped at the interface, form a tunnel barrier layer, form a depletion layer with negative space charge or can be exchanged and recombined with an additional oxygen reservoir layer. Remarkably, for the PCMO based devices Dittmann's group was able to experimentally prove the occurrence of this bias-induced oxygen drift and concomitant redox reactions by spectroscopic techniques.[31,32] By using hard X-ray photoelectron spectroscopy (HAXPES) they showed that when yttria-stabilized zirconia (YSZ) is on top of PCMO, an exchange of oxygen ions between the two oxides causes the resistance change, determined by the electrostatic charging of YSZ.[31] On the other hand, if a reactive metal electrode such as Ti is deposited on top of PCMO, the change in resistance occurs by the formation and shortening of an insulating tunnel barrier due to a reversible redox-reaction at the interface. In addition to mixed-valence manganites, we have recently shown that cobaltites, and in particular $GdBaCo_2O_{5+\delta}$ (GBCO), also presents area-dependent switching characteristics, when built as single devices[39] or as symmetric devices in back-to-back configuration.[40] The memristive cells were engineered by sandwiching GBCO between Ag and $LaNiO_3$. In this case a superposition of volume RS (variation of the GBCO resistivity due to a change in oxygen content) and interface type RS (creation of an electronic and ionic conduction interface barrier) were responsible for the observed non-volatile change of resistance.

In this work we selected $La_2NiO_{4+\delta}$ (L2NO4), a MIEC oxide, as oxygen storage and transport medium with the aim of controlling the interface-type switching and of obtaining analog-type resistance changes (instead of two well defined states). On the one hand, L2NO4 was chosen due to its high oxygen mobility, as a better control over the oxygen drift and diffusion increases the likelihood of

Journal of Materials Chemistry C
View Article Online
DOI: 10.1039/C9TC03972D

obtaining an analog memory behavior, which is key for neuromorphic computing.[23] While oxygen vacancies are usually the migrating dopant defects in the majority of the oxides used as memristive media, in L2NO4 interstitial oxygen ions have to be considered instead. L2NO4 is among the materials with highest diffusion coefficients at intermediate temperatures combined with a low activation energy,[41,42] and could therefore present significant oxygen diffusion near room temperature. A comparative figure including literature diffusion coefficients of relevant memristive and good ionic conducting oxides, together with extrapolated characteristic diffusion length values is shown in **Figure S1**. On the other hand, L2NO4 is also a good electronic conductor, key in the hopes of achieving a homogeneous change in resistance located at the electrode/oxide interface. Thus the contact resistance between the electrode and the sandwiched L2NO4 will depend mainly on the presence or absence of insulating interfacial layers (e.g. partial oxidation of the electrode) and/or from space-charge regions which can develop in certain band-alignment conditions (between the metallic electrode and the semiconducting switching layer) forming a Schottky contact.[17,26]

In this work we have built memristive analog devices in which an active n-p junction was artificially created by putting in contact a MIEC, p-type semiconducting active material (L2NO4) with an n-type TiO_{2-y} interlayer (formed during the evaporation of the Ti top electrode). An ohmic (inactive) contact was formed when using a Pt counter electrode, effectively concentrating the voltage drop at the Ti/L2NO4 interface. A very gradual, highly multilevel analog change in resistance was obtained for this asymmetric Pt/L2NO4/Ti heterostructure both for the set and for the reset transitions. The devices show rectifying I(V) characteristics, interesting to suppress current sneak-path and memory cross-talk issues in memristor crossbar arrays.[43] In addition, history-dependent memory relaxation dynamics have been measured. After having programmed the devices to a HRS, the resistance spontaneously continues increasing first, before relaxing back to a LRS. The relaxation to LRS is

Journal of Materials Chemistry C
View Article Online
DOI: 10.1039/C9TC03972D

faster when the memory is programmed with alternating bipolar voltage pulses than when left unstimulated. Finally, a phenomenological band diagram-based model based on the experimental evidence gathered from the structural, chemical and electrical measurements is proposed as a visual tool to explain the measured memory dynamics for this Pt/L2NO4/Ti memristive heterostructure.

L2NO4 is the first member of the Ruddlesden-Popper series with general formula $La_{n+1}Ni_nO_{3n+1}$. As shown in **Figure 1.a**, L2NO4 is best described as an alternation along the *c* crystallographic direction of $LaNiO_3$ perovskite blocks and LaO rock salt layers rotated by 45° in the basal plane of the parent tetragonal structure. In L2NO4 interstitial oxygen ions act as negatively-charged point defects, they are both mobile and electrically active, effectively acting as mobile acceptor dopants through a self-doping mechanism, giving rise to the p-type semiconducting behavior reported for this material. They are located in the LaO rock-salt layers and diffuse along that plane through an interstitialcy mechanism.[44] The crystal quality of L2NO4 films deposited on $SrTiO_3$ (STO) by Pulsed-injection Metal Organic Vapor Deposition (PiMOCVD) can be observed in **Figure 1.b**. The out of plane θ-2θ X-ray diffraction (XRD) patterns only show the 0 0 *l* (*l* even) Bragg reflections of tetragonal L2NO4 in addition to the *h* 0 0 (*h* integer) STO substrate peaks. The film is approximately 67 nm thick as measured by X-Ray Reflectometry (XRR) and confirmed by TEM. The high-resolution TEM cross-section image taken at the L2NO4/STO interface (**Figure 1.c**) shows the alternating $LaNiO_3$ and LaO layers (horizontal fringes) stacked parallel to the substrates surface along the *c* crystallographic direction of L2NO4.

The electrical (I-V) characteristics for the different pairs of electrodes (Pt-Pt, Pt-Ag and Ag-Ag) displayed in **Figure 1.d** clearly show an evolution of the transport properties across the M/L2NO4 heterojunction from an ohmic contact for Pt, the metal with the highest work function (WF = 5.65 eV) to a more nonlinear Schottky-like contact for Ag, with a lower WF (4.26 eV). These results are

Journal of Materials Chemistry C
View Article Online
DOI: 10.1039/C9TC03972D

coherent with the creation of a p-type Schottky barrier for L2NO4. Moreover, the significant current decrease shown in the I-V characteristics for electrode pairs containing at least one Ti electrode (Figure 1.d) cannot be explained by a conventional metal/semiconductor (M/SC) Schottky contact since Ag and Ti have similar work functions (4.26 eV and 4.33 eV, respectively). The observed increase in resistance suggest that, as expected, a TiO_x interlayer formed at the Ti/L2NO4 interface, effectively turning the initial Ti/L2NO4 into a Ti/TiO_x/L2NO4 heterojunction. The spontaneous oxidation of Ti electrodes during the processing steps, mentioned in several research articles, is attributed to the high oxygen affinity of the metal.[45,46]

The presence of a TiO_x interlayer has been confirmed by transmission electron microscopy (TEM), by analyzing the cross-section of selected regions of interest below both electrodes. The HAADF TEM image of the Pt/L2NO4/STO half device (**Figure 1.e**) clearly shows the presence of the three expected layers: bottom STO substrate, L2NO4 thin film and top evaporated Pt electrode. In the case of the Ti/L2NO4/STO half device (**Figure 1.f**), these three layers (electrode/film/substrate) are also present, but an additional darker contrast is observed between Ti and L2NO4. The presence of an oxygen-rich TiO_x interlayer, which is otherwise absent at the Pt/L2NO4 interface, is put in evidence by superimposing the TEM cross-section images with the electron-energy loss spectroscopy (EELS) chemical profiles for O and Ti. By calibrating the intensity of the two profiles using the 3:1 oxygen to titanium stoichiometry for the $SrTiO_3$ substrate, a TiO_{2-y} with $y \approx 0.3$ has been estimated for interface region (oxygen peak) near the Ti electrode (see Figure S2 and corresponding text in the supplementary information for more details). A highly sub-stoichiometric TiO_{2-y} interlayer is thus present in the pristine (unbiased) state of the device.

The application of negative voltage pulses to the Pt electrode sets a pristine Pt/L2NO4/Ti device in a high resistance state (HRS), reaching a resistance value more than two orders of magnitude higher

Journal of Materials Chemistry C
View Article Online
DOI: 10.1039/C9TC03972D

than the pristine one. **Figure 2.a** shows the evolution of the resistance-voltage (R-V) characteristics (from -1 to 1 V) at different stages of the experiment consisting in the successive application of increasing voltage pulses. The device initially shows non-linear and slightly rectifying electrical characteristics (stage 1, R = 878 kΩ, measured at +10 mV). The device is then stressed electrically by applying successive negative voltage pulses (of 100 s duration) of increasing amplitude, from -1 up to -5 V (see **Figure S3**). After the -3 V pulse the device shows an increase in resistance and an apparent increase in ohmicity (Figure 2.a, stage 2), likely due to an increase in the built-in potential, translating into an increase in the threshold voltage, under which the thermally-generated carriers ensure an ohmic-like conduction. A more substantial increase in resistance is achieved after the stress at -4 V and -5 V (Figure 2.a, stages 3 and 4, respectively). The change in resistance is history-dependent as the subsequent application of a-5 V pulse increases the resistance of the device even further (stage 5). The new HRS of the device is then subjected to bipolar voltage sweeps ($\pm V_{max}$), increasing the maximum voltage (V_{max}) every five cycles (**Figure S4.a-c**, Supporting Information). Interestingly, an additional resistance relaxation in which both the HRS and the LRS decrease over time is present and can be clearly observed after each new I(V) cycle. This resistance relaxation will be further described in **Figure 3.** The highly reproducible R-V and I-V characteristics (at ±5 V) of the Pt/L2NO4/Ti devices and their eightwise memristive behavior are shown in **Figure 2.b** and **c**, respectively, presenting very little variability and an analog transition between resistance states. The HRS and the LRS are both rectifying, suggesting that the underlying carrier transport mechanism might not have changed between the two states. The HRS features a large built-in potential (threshold voltage) that decreases when programming the device to the LRS (after a 0 → +5 V voltage sweep). Then, when the voltage is swept in the reverse bias, the modulus of the current increases until it reaches a maximum around -2.75 V (inset in Figure 2.d), after which the current gradually decreases.

Journal of Materials Chemistry C
View Article Online
DOI: 10.1039/C9TC03972D

This gradual decrease (increase) in current offers the opportunity of controlling the HRS (LRS) value in a very precise manner, which is hard to achieve in filamentary-based memristive systems in which the set transition (change between HRS and LRS) is very fast and abrupt (occurring in a narrow voltage range). In addition, **Figure 2.d** shows how the device can be gradually programmed to a lower or higher resistance state by applying successive positive or negative unipolar voltage sweeps, respectively. The device shows highly multilevel bipolar programing capabilities when operated with voltage pulses, its resistance state can be finely tuned by changing the number of pulses, their duration and/or their amplitude (**Figure 2.e** and **Figure 2.f**).

Remarkably, the device shows a unique dynamic relaxation behavior. Indeed, after having programmed the device from an IRS of 1.5 MΩ to a HRS of 32 MΩ, its resistance continues to spontaneously increase by more than an order of magnitude (up to 766 MΩ) during approximately 720 s after the application of the last programming pulse ("Relax 1" **Figure 3.a**). The magnitude and duration of this spontaneous increase in resistance depends on the biasing history of the device, eventually reaching a maximum before slowly relaxing back to a LRS ("Relax 2" in Figure 3.a). As illustrated in **Figure 2.e**, the larger the amplitude of the previously applied pulses, the larger the spontaneous increase in resistance ("Relax 1"), varying in this case from 1.5 kΩ/s to 105 kΩ/s after the -5 and -10 V train of pulses, respectively. It should be noticed that if during the "Relax 1" process a train of alternating positive and negative voltage pulses is applied (**Figure 3.b**), the spontaneous increase is reversed and the device rapidly relaxes back (from ~130 MΩ to ~1 MΩ) towards a LRS which is close to the initial resistance state. The memory thus has a transient behavior both if left unbiased for a certain duration (slower "forgetting", Figure 3.a), but also if it receives contradictory information, represented here by the alternating bipolar voltage pulses (faster "forgetting", Figure 3.b). Furthermore, the programmed change in resistance depends both on the pulse characteristics

Journal of Materials Chemistry C
View Article Online
DOI: 10.1039/C9TC03972D

and on the programming history. Indeed, when reiterating identical pulses [-10 V; 1500 ms] a second time, as illustrated for the -10 V pulse sequence in Figure 3.b and Figure S5 (logarithmic scale), the resistance increase per pulse becomes larger, i.e., it becomes easier to program the device to HRS. However, the spontaneous resistance increase that follows when removing the electrical field (Relax 1) is less important, and the device quickly enters the "forgetting" regime (Relax 2). The fact that identical pulse characteristics do not lead to a fixed change in resistance (for a given initial resistance state) puts into evidence the history dependent memory characteristics of this device.

The electrochemical mechanisms, ion drift (due to an electrical potential gradient) and diffusion (due to a chemical concentration gradient) processes and related band diagrams which qualitatively describe the interface-type resistance changes and dynamic behavior measured for the Pt/L2NO4/Ti devices are shown in **Figure 3.c**. Upon evaporation of the Ti electrode, a n-p junction is expected to form between an amorphous oxygen deficient TiO_{2-y} phase (n-type) and the oxygen hyperstoichiometric L2NO4 phase (p-type semiconductor), resulting in a Ti/TiO_{2-y}/L2NO4 heterojunction (band alignment sketch presented in **Figure 3.c.1**). As the Pt/L2NO4 and the Ti/TiO_{2-y} contacts are ohmic,[12] here we focus only on the TiO_{2-y}/L2NO4 n-p heterojunction. In thermal equilibrium (**Figure 3.c.1**) the alignment of the different Fermi levels across the entire M/n-SC/p-SC stack results in an upwards and downwards band-bending of n-TiO_{2-y} and p-L2NO4, respectively. The resulting majority carrier depletion regions in both materials concentrate most of the voltage drop across the junction. Upon application of an optimized negative voltage pulse (or train of pulses), the negatively charged oxygen interstitials (O_i'') gain sufficient energy to drift from the bulk of L2NO4 towards the grounded Ti electrode (**Figure 3.c.2**). When the bias is removed, the system is in a non-equilibrium state (**Figure 3.c.3**) and an important dopant gradient exists on the L2NO4 side. Indeed, the O_i'' point defects act as mobile acceptor dopants, locally generating hole carriers to ensure charge

Journal of Materials Chemistry C
View Article Online
DOI: 10.1039/C9TC03972D

neutrality within L2NO4. The opposite is true for TiO_{2-y}, where positively-charged oxygen vacancies $V_O^{\bullet\bullet}$ act as donor defects. The increase in hole carriers at the surface of L2NO4 due to the external field-induced accumulation of O_i'' decreases its Fermi energy and shrinks the depletion width. This has the double effect of increasing the built-in potential at the TiO_{2-y}/L2NO4 junction and localizing the voltage drop on a shorter distance (effectively increasing the electric field across the n-p junction). Two scenarios are then possible: if the device remains unbiased the O_i'' species diffuse away from the TiO_{2-y}/L2NO4 interface and back into the L2NO4 bulk (**Figure 3.c.4)**. This diffusion is triggered by the re-equilibration of the O_i'' concentration gradient within L2NO4 through a Fickian diffusion process, leading to a relaxation of the device to the previous equilibrium state (**Figure 3.c.1**).

In the second scenario, a new negative voltage pulse is applied on the L2NO4 side (**Figure 3.c.5**) and, if the oxygen ions did not have the time to re-equilibrate, the interfacial region is doped further. The previous process (decrease of the Fermi level and depletion width) is reiterated, further increasing the built-in potential and the electric field across the n-p junction. At a certain oxygen ion concentration threshold, the applied voltage - now strongly assisted by the large internal electric fields - is able to trigger the drift of oxygen ions from the p-L2NO4 side to the n-TiO_{2-y} side (**Figure 3.c.5**). This process can be described as a reduction of L2NO4 concomitant to the oxidation of TiO_{2-y}:

$$La_2NiO_{4+\delta} + TiO_{2-y} \rightarrow La_2NiO_{4+\delta-x} + TiO_{2-y+x} \quad (1)$$

Both mass transport (oxygen ions from L2NO4 to TiO_{2-y}) and charge transfer (from Ni to Ti) can be rate-limiting, but a mass-transport limited chemical reaction could explain the more gradual analog-type change in resistance measured in these devices (when compared to the majority of filamentary switching characteristics reported in literature). The formation and growth of the insulating TiO_2 thin

Journal of Materials Chemistry C
View Article Online
DOI: 10.1039/C9TC03972D

film will take place until the electric field generated by the driving force is compensated by the resistance drop in the oxide.[47] This can explain the apparent saturation behavior when carrying-out unipolar negative sweeps (**Figure S6**). A particularly interesting feature of this redox reaction (**Equation 1)** is that two point defects are simultaneously annihilated together with their charge-compensating electric carriers ($2h^{\bullet}$ for O_i'' and $2e'$ for $V_O^{\bullet\bullet}$). Thus a "de-doping" process occurs simultaneously in both materials composing the n-p junction, which can explain the gradual change in resistance discussed earlier (inset in Figure 2.c), where an increase in negative electric field led to a decrease in current due to the simultaneous loss of n and p charge carriers available at the TiO_{2-y}/L2NO4 junction. The annihilation of oxygen vacancies in TiO_{2-y} has also been evoked as being the reason for the resistance increase in a Pt/TiO_2/Pt memristive device.[48] Finally, after this voltage-pulse-induced redox process, the device is in a higher resistance state (**Figure 3.c.6**). It is then possible to control the kinetics of the change to a lower resistance state either by applying a positive voltage pulse (fast) or without further stimulation (spontaneous relaxation, slower kinetics). The resistance decrease can be related to the reduction of the TiO_x interlayer (thickness and/or stoichiometry) and the release of oxygen ions, which diffuse back into L2NO4 (dotted arrow from **Figure 3.c.6** to 3.c.4) together with the increase in the carrier concentration (both in TiO_x and L2NO4). Since the free energy of oxidation of Ti is very low in close to room-temperature conditions (the ΔG_{ox} (300K) of the reaction $Ti + O_2 \rightarrow TiO_2$ is of approx. -800 kJ/mol),[49] only few materials can spontaneously reduce the very stable TiO_2 oxide. However, less energy is required to partially reduce TiO_x as the free energy of oxidation of partially oxidized TiO_{2-y} into stoichiometric TiO_2 is much larger, i.e. -200 kJ/mol.[49] On the other hand, stoichiometric $La_2NiO_{4.00}$ is highly unstable and can only be obtained in highly reducing conditions. [50] If a hole-depletion region exists at the L2NO4 side of the Ti/L2NO4 junction, there should be a concomitant local absence of interstitial oxygen dopants. This 'highly

Journal of Materials Chemistry C
View Article Online
DOI: 10.1039/C9TC03972D

reduced' $La_2NiO_{4.00}$ interfacial region could then partially reduce TiO_{2-y} where the two materials are in contact. Another possibility is that some of the oxygen ions that drifted into the Ti electrode have not reacted chemically with it and could be adsorbed at the surface or inside the grain boundaries, as has been proposed for the Ti electrode in graphene-oxide memristive devices.[51] This adsorbed oxygen could then easily be released and reincorporated into L2NO4. In both cases the TiO_x (TiO_{2-y} or TiO_2) interlayer loses oxygen atoms which likely play the role of electron traps at the TiO_x/L2NO4 interface. This oxygen loss can, on top of releasing trapped electrons and increasing the overall carrier density, also restore other conduction mechanisms through the TiO_x interlayer (such as TAT or direct tunneling if the layer is thin enough), which effectively also decreases the resistance of the device. The ion drift process is certainly temperature activated, and thus an increase in the pulse duration, amplitude or number could assist the aforementioned resistance change mechanism through Joule heating. Furthermore, the presence of electrochemical redox reactions explains the polarity-dependent memristive properties of the device, as reversing the voltage polarity changes the role of the electrodes, effectively inverting the reaction described in **Equation 1**.

To conclude, a p-type semiconducting MIEC has been used to build an artificial synapse with analog, highly multilevel set and reset transitions and built-in memory transience. The observed memory behavior has been explained with the generation of an active p-n junction between p-type L2NO4 and n-type TiO_x where oxygen mass transport between the two materials induces a gradual and reversible change of the junction properties. A de-doping process occurring simultaneously in both materials upon oxygen exchange increases the carrier depletion widths on both sides of the TiO_x/L2NO4 junction while forming an increasingly insulating TiO_x interlayer. The low temperature oxygen-diffusion capabilities of L2NO4 allow for an important ionic re-equilibration and a transient memory behavior through field, temperature and concentration-gradient activated diffusion mechanisms. It is

Journal of Materials Chemistry C
View Article Online
DOI: 10.1039/C9TC03972D

clear that this complex-oxide based memristive hererostructure would require non trivial programing solutions in order to become technologically relevant. Still, these exciting experimental results open the avenue to the design of a plethora of novel memristive nanoionic devices with tuned gradual resistance change and memory transience. New artificially created and tunable p-n junctions between bilayers of mixed ionic electronic p-type oxides and n-type "oxygen-reservoir" oxides should be explored. Their future miniaturization and integration into high-density cross-bar array designs offers great potentiality in technologically relevant neuromorphic hardware with short-term synaptic dynamics and unsupervised learning capabilities.

Journal of Materials Chemistry C
View Article Online
DOI: 10.1039/C9TC03972D

Experimental Section: L2NO4-based thin films (~67 nm) were deposited on $SrTiO_3$. The 10x10 cm² (100)$SrTiO_3$ single crystal substrates, one side polished were purchased from Crystec and followed a mild 3-step cleaning process (acetone, isopropanol, deionized water) in an ultrasonicating bath, followed by the deposition of the L2NO4 film by PiMOCVD (deposition conditions are detailed in **Table S1**). The electrical contacts were fabricated by e-beam induced metal evaporation (MEB550 from PLASSYS) using a laser-assisted lithography process (μPG 101 from HEIDELBERG Instruments) in cleanroom facilities. A mild Ar^+ etch was used to prepare the exposed surface of the patterned sample and remove potential left-overs of the photoresist before metal evaporation. Three metals with different work functions were evaporated (Pt, Ag and Ti), forming square pads of 200x200 μm².

Phase identification, structural and crystallinity characterization of the samples were performed using X-ray diffraction (XRD) in θ-2 θ geometry (Bruker D8 Advance) with monochromatic $CuK_{\alpha 1}$ radiation (λ = 1.5406 Å). The film thickness was determined by X-Ray Reflectometry (XRR) with a RIGAKU Smartlab diffractometer.

A JEOL 2010 microscope operated at 200 kV with a beam current of 110 μA was used for high resolution TEM (HRTEM) characterization. The samples were prepared with the MultiPrep™ system (Allied High Tech Products, Inc.). The final thinning of the TEM lamella was performed by a precision ion polishing system (PIPS, 691 model) with a milling angle of ±7° at 2.8 KeV and 500 eV. The lamellas for the STEM/EELS experiments were prepared by Focused Ion Beam (FIB) using a FEI strata 400S equipped with a dual beam electron/Ga^+ ions. The region of interest is thinned to approximately 100 nm using a decreasing acceleration, from 16 kV to 2 kV to limit the amorphization of the sample. The high resolution STEM images and the Electron Energy Loss Spectroscopy (EELS) have been acquired on a FEI TITAN Themis microscope with an electron acceleration of 200 kV.

Journal of Materials Chemistry C
View Article Online
DOI: 10.1039/C9TC03972D

The microscope is probe corrected, and is equipped with a Gatan Image Filter (GIF) Quantum with a CCD camera of 2048x256 pixels allowing dual EELS. This GIF is monitored by Gatan Microscope Suite 3 (GMS 3). The pixel size for the EELS maps was set to 1.5 nm. The element profiles have been obtained by integrating the area bellow the respective edges using a conventional GMS 3 data treatment.

Current-Voltage (I-V) characteristics were obtained using a source-measurement unit (Agilent B1500) using two tungsten-carbide probes operated in a voltage-control mode in a Karl-Suss probe station. In all the I-V plots shown, the voltage was applied on the Pt electrode while the counter electrode (either Ag or Ti) was grounded. The bipolar sweeps always start at zero bias and go as follows: 0 V → $+V_{max}$ → 0 V → $-V_{min}$ → 0 V, with a constant sweeping rate of ~350 mV/s. The resistance values extracted from the I-V curves were always calculated at V = +10 mV. Current-time (I-t) characteristics when operated in "pulsed mode" consist in applying a voltage stress to program the device to a higher or lower resistance state, applying either a positive or negative voltage on the Pt electrode while keeping the Ti counter electrode grounded, respectively. The remnant resistance state of the device is then readout after each programing pulse at a lower V = +10 mV bias to ensure that no ionic movement would be triggered by the electrical field. All the electrical measurements were carried out in ambient conditions.

Supporting Information

Supporting Information is available.

Conflicts of interest

There are no conflicts to declare.

Journal of Materials Chemistry C
View Article Online
DOI: 10.1039/C9TC03972D

Acknowledgements

This work has been partially supported by the LabEx Minos ANR-10-LABX-55-01 and by two ANR funded projects MICROSWITCH (ANR-14-ACHN-0012) and Alps Memories (ANR-15-CE24-0018). In addition, the work has been performed with the help of the ‘‘Plateforme Technologique Amont’’ of Grenoble, with the financial support of the ‘‘Nanosciences aux limites de la Nanoélectronique’’ Fundation and CNRS Renatech network and has benefited from the facilities and expertise of the OPE)N(RA characterization platform of FMNT (FR 2542, fmnt.fr) supported by CNRS, Grenoble INP and UGA. K. Momma and F. Izumi are kindly acknowledged for the creation of VESTA[52].

References:

1 S. D. Ha and S. Ramanathan, *J. Appl. Phys.*, 2011, **110**, 071101.

2 P.-Y. Deng and V. A. Klyachko, *Commun. Integr. Biol.*, 2011, **4**, 543–548.

3 S. Yu, B. Gao, Z. Fang, H. Yu, J. Kang and H. S. P. Wong, *Adv. Mater.*, 2013, **25**, 1774–1779.

4 S. G. Kim, J. S. Han, H. Kim, S. Y. Kim and H. W. Jang, *Adv. Mater. Technol.*, 2018, **1800457**, 1800457.

5 Z. Sun, E. Ambrosi, A. Bricalli and D. Ielmini, *Adv. Mater.*, 2018, **30**, 1–8.

6 Z. Wang, S. Joshi, S. Savel’ev, W. Song, R. Midya, Y. Li, M. Rao, P. Yan, S. Asapu, Y. Zhuo, H. Jiang, P. Lin, C. Li, J. H. Yoon, N. K. Upadhyay, J. Zhang, M. Hu, J. P. Strachan, M. Barnell, Q. Wu, H. Wu, R. S. Williams, Q. Xia and J. J. Yang, *Nat. Electron.*, 2018, **1**, 137–145.

7 F. M. Bayat, M. Prezioso, B. Chakrabarti, H. Nili, I. Kataeva and D. Strukov, *Nat. Commun.*, 2018, **9**, 2331.

Journal of Materials Chemistry C
View Article Online
DOI: 10.1039/C9TC03972D

8 M. Prezioso, F. Merrikh-Bayat, B. D. Hoskins, G. C. Adam, K. K. Likharev and D. B. Strukov, *Nature*, 2015, **521**, 61–64.

9 D. S. Jeong and C. S. Hwang, *Adv. Mater.*, 2018, **30**, 1–27.

10 N. K. Upadhyay, H. Jiang, Z. Wang, S. Asapu, Q. Xia and J. Joshua Yang, *Adv. Mater. Technol.*, 2019, **4**, 1–13.

11 S. Munjal and N. Khare, *Sci. Rep.*, 2017, **7**, 12427.

12 J. J. Yang, M. D. Pickett, X. Li, D. A. A. Ohlberg, D. R. Stewart and R. S. Williams, *Nat. Nanotechnol.*, 2008, **3**, 429–33.

13 R. Berdan, E. Vasilaki, A. Khiat, G. Indiveri, A. Serb and T. Prodromakis, 2015, 1–17.

14 T. Ohno, T. Hasegawa, T. Tsuruoka, K. Terabe, J. K. Gimzewski and M. Aono, *Nat. Mater.*, 2011, **10**, 591–595.

15 B. A. Richards and P. W. Frankland, *Neuron*, 2017, **94**, 1071–1084.

16 G.-L. Li, J. J. Yang, Q. Xia, Z. Wang, P. Lin, M. Hu, M. Barnell, S. E. Savel'ev, Q. Wu, N. Ge, Z. Li, H. L. Xin, R. Midya, J. P. Strachan, H. Jiang, S. Joshi and R. S. Williams, *Nat. Mater.*, 2016, **16**, 101–108.

17 S. Bagdzevicius, K. Maas, M. Boudard and M. Burriel, *J. Electroceramics*, 2017, **39**, 157–184.

18 A. Marchewka, B. Roesgen, K. Skaja, H. Du, C.-L. Jia, J. Mayer, V. Rana, R. Waser and S. Menzel, *Adv. Electron. Mater.*, 2016, **2**, 1500233.

19 S. Yu, Y. Wu, R. Jeyasingh, D. Kuzum and H. S. P. Wong, *IEEE Trans. Electron Devices*, 2011, **58**, 2729–2737.

20 S. Larentis, F. Nardi, S. Balatti, D. C. Gilmer and D. Ielmini, *IEEE Trans. Electron Devices*, 2012, **59**, 2468–2475.

Journal of Materials Chemistry C
View Article Online
DOI: 10.1039/C9TC03972D

21 B. Sarkar, B. Lee and V. Misra, *Semicond. Sci. Technol.*, , DOI:10.1088/0268-1242/30/10/105014.

22 J. Joshua Yang, F. Miao, M. D. Pickett, D. A. A. Ohlberg, D. R. Stewart, C. N. Lau and R. S. Williams, *Nanotechnology*, 2009, **20**, 215201.

23 Y. Li, Z. Wang, R. Midya, Q. Xia and J. J. Yang, *J. Phys. D. Appl. Phys.*, 2018, **51**, 503002.

24 Z. Wu, J. Wei, R. Cao, X. Zhang, S. Long, X. Zhao, Q. Liu, T. Shi, M. Liu, W. Wang, J. Lu and R. Wang, *Materials (Basel).*, 2018, **11**, 2102.

25 R. Chen, W. Hu, L. Zou, W. Xie, B. Li and D. Bao, *Appl. Phys. Lett.*, 2014, **104**, 242111.

26 A. Sawa and R. Meyer, in *Resistive Switching*, Wiley-VCH Verlag GmbH & Co. KGaA, Weinheim, Germany, 2016, pp. 457–482.

27 R. Ortega-Hernandez, M. Coll, J. Gonzalez-Rosillo, A. Palau, X. Obradors, E. Miranda, T. Puig and J. Suñe, *Microelectron. Eng.*, 2015, **147**, 37–40.

28 J. C. Gonzalez-Rosillo, R. Ortega-Hernandez, B. Arndt, M. Coll, R. Dittmann, X. Obradors, A. Palau, J. Suñe and T. Puig, *Adv. Electron. Mater.*, 2019, 1800629.

29 Y. B. Nian, J. Strozier, N. J. Wu, X. Chen and A. Ignatiev, *Phys. Rev. Lett.*, 2007, **98**, 146403.

30 A. Sawa, *Mater. Today*, 2008, **11**, 28–36.

31 C. Baeumer, T. Heisig, B. Arndt, K. Skaja, F. Borgatti, F. Offi, F. Motti, G. Panaccione, R. Waser, S. Menzel and R. Dittmann, *Faraday Discuss.*, 2019, **213**, 215–230.

32 A. Herpers, C. Lenser, C. Park, F. Offi, F. Borgatti, G. Panaccione, S. Menzel, R. Waser and R. Dittmann, *Adv. Mater.*, 2014, **26**, 2730–5.

33 Z. L. Liao, P. Gao, Y. Meng, H. W. Zhao, X. D. Bai, J. D. Zhang and D. M. Chen, *Appl. Phys. Lett.*, 2011, **99**, 113506.

34 Y. Jin, Z. Xu, K. Jin, X. He, C. Wang and H. Lu, *Phys. B Condens. Matter*, 2014, **449**, 52–56.

Journal of Materials Chemistry C
View Article Online
DOI: 10.1039/C9TC03972D

35 K. Moon, A. Fumarola, S. Sidler, J. Jang, P. Narayanan, R. M. Shelby, G. W. Burr and H. Hwang, *IEEE J. Electron Devices Soc.*, 2018, **6**, 146–155.

36 A. Fumarola, S. Sidler, K. Moon, J. Jang, R. M. Shelby, P. Narayanan, Y. Leblebici, H. Hwang and G. W. Burr, *IEEE J. Electron Devices Soc.*, 2018, **6**, 169–178.

37 J.-W. Jang, S. Park, Y.-H. Jeong and H. Hwang, in *2014 IEEE International Symposium on Circuits and Systems (ISCAS)*, IEEE, 2014, pp. 1054–1057.

38 K. Moon, S. Park, J. Jang, D. Lee, J. Woo, E. Cha, S. Lee, J. Park, J. Song, Y. Koo and H. Hwang, *Nanotechnology*.

39 S. Bagdzevicius, M. Boudard, J. M. Caicedo, L. Rapenne, X. Mescot, R. Rodríguez-Lamas, F. Robaut, J. Santiso and M. Burriel, *J. Mater. Chem. C*, 2019, **7**, 7580–7592.

40 S. Bagdzevicius, M. Boudard, J. Manuel and X. Mescot, *Solid State Ionics*, 2019, **334**, 29–35.

41 M. Burriel, G. Garcia, J. Santiso, J. A. Kilner, R. J. Chater and S. J. Skinner, *J. Mater. Chem.*, 2008, **18**, 416–422.

42 R. Sayers, R. A. De Souza, J. A. Kilner and S. J. Skinner, *Solid State Ionics*, 2010, **181**, 386–391.

43 J. S. Lee, S. Lee and T. W. Noh, *Appl. Phys. Rev.*, 2015, **2**, 031303.

44 A. Chroneos, D. Parfitt, J. A. Kilner and R. W. Grimes, *J. Mater. Chem.*, 2010, **20**, 266.

45 F. Borgatti, C. Park, A. Herpers, F. Offi, R. Egoavil, Y. Yamashita, A. Yang, M. Kobata, K. Kobayashi, J. Verbeeck, G. Panaccione and R. Dittmann, *Nanoscale*, 2013, **5**, 3954–60.

46 K. Shono, H. Kawano, T. Yokota and M. Gomi, *Appl. Phys. Express*, 2008, **1**, 0550021–0550023.

47 I. Valov and R. Waser, in *Resistive Switching: From Fundamentals of Nanoionic Redox Processes to Memristive Device Applications*, 2016, pp. 253–287.

Journal of Materials Chemistry C
View Article Online
DOI: 10.1039/C9TC03972D

48 D. S. Jeong, H. Schroeder, U. Breuer and R. Waser, *J. Appl. Phys.*, , DOI:10.1063/1.3043879.

49 J. J. Yang, J. P. Strachan, F. Miao, M. X. Zhang, M. D. Pickett, W. Yi, D. A. A. Ohlberg, G. Medeiros-Ribeiro and R. S. Williams, *Appl. Phys. A Mater. Sci. Process.*, 2011, **102**, 785–789.

50 M. Sayer and P. Odier, *J. Solid State Chem.*, 1987, **67**, 26–36.

51 V. K. Nagareddy, M. D. Barnes, F. Zipoli, K. T. Lai, A. M. Alexeev, M. F. Craciun and C. D. Wright, *ACS Nano*, 2017, **11**, 3010–3021.

52 K. Momma and F. Izumi, *J. Appl. Crystallogr.*, 2011, **44**, 1272–1276.

Journal of Materials Chemistry C
View Article Online
DOI: 10.1039/C9TC03972D

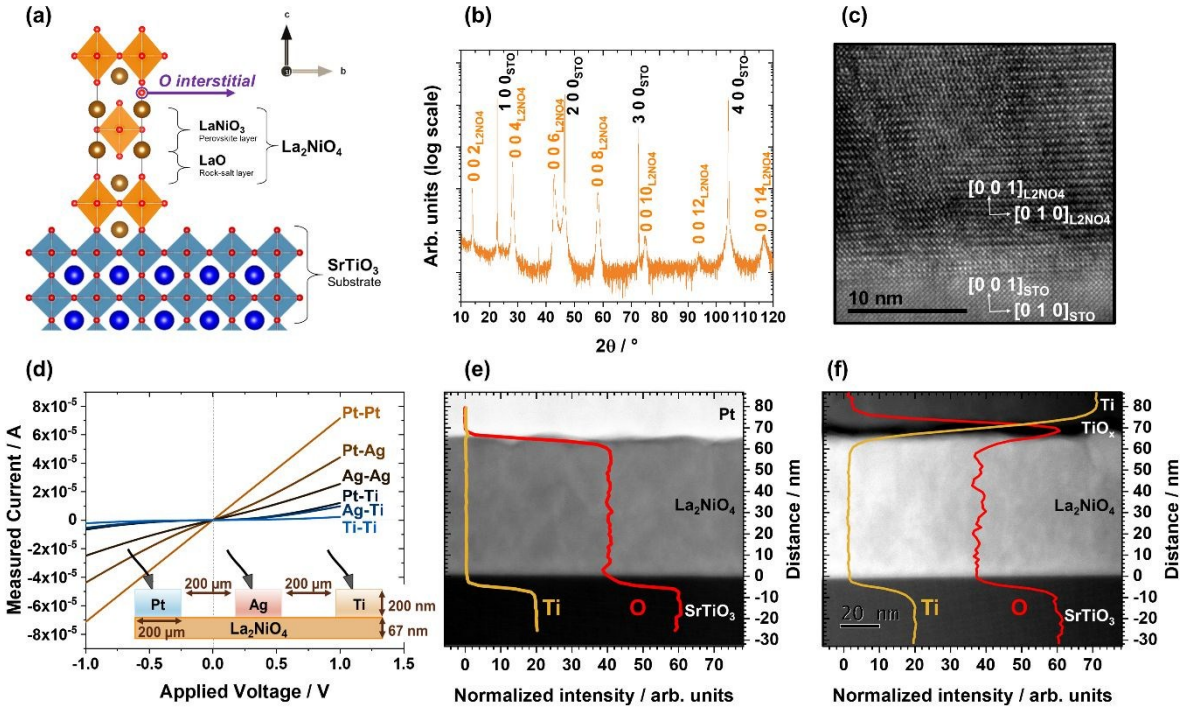

Figure 1: (a) Schematic of the L2NO4/STO epitaxial heterostructure (orange diamonds represent Ni-centered oxygen octahedra) and location of the mobile interstitial oxygen in the LaO rock-salt layer. (b) θ -2θ XRD pattern of L2NO4/STO showing a highly oriented L2NO4 film (*c*-axis pointing out of plane). (c) HRTEM cross-section image taken at the L2NO4/STO interface. (d) I-V characteristics (±1 V) for different metal/L2NO4/metal heterojunctions. (e, f) HAADF TEM images of a pristine Pt/L2NO4/Ti device cross-section taken under a Pt electrode and a Ti electrode, respectively. A darker contrast (lower density) can be seen at the Ti/L2NO4 interface. Chemical profiles for oxygen (red) and titanium (yellow) are superimposed to the images. These profiles were measured by EELS and have been normalized in intensity to the STO substrate. The L2NO4 thin film is ~67 nm thick.

Journal of Materials Chemistry C
View Article Online
DOI: 10.1039/C9TC03972D

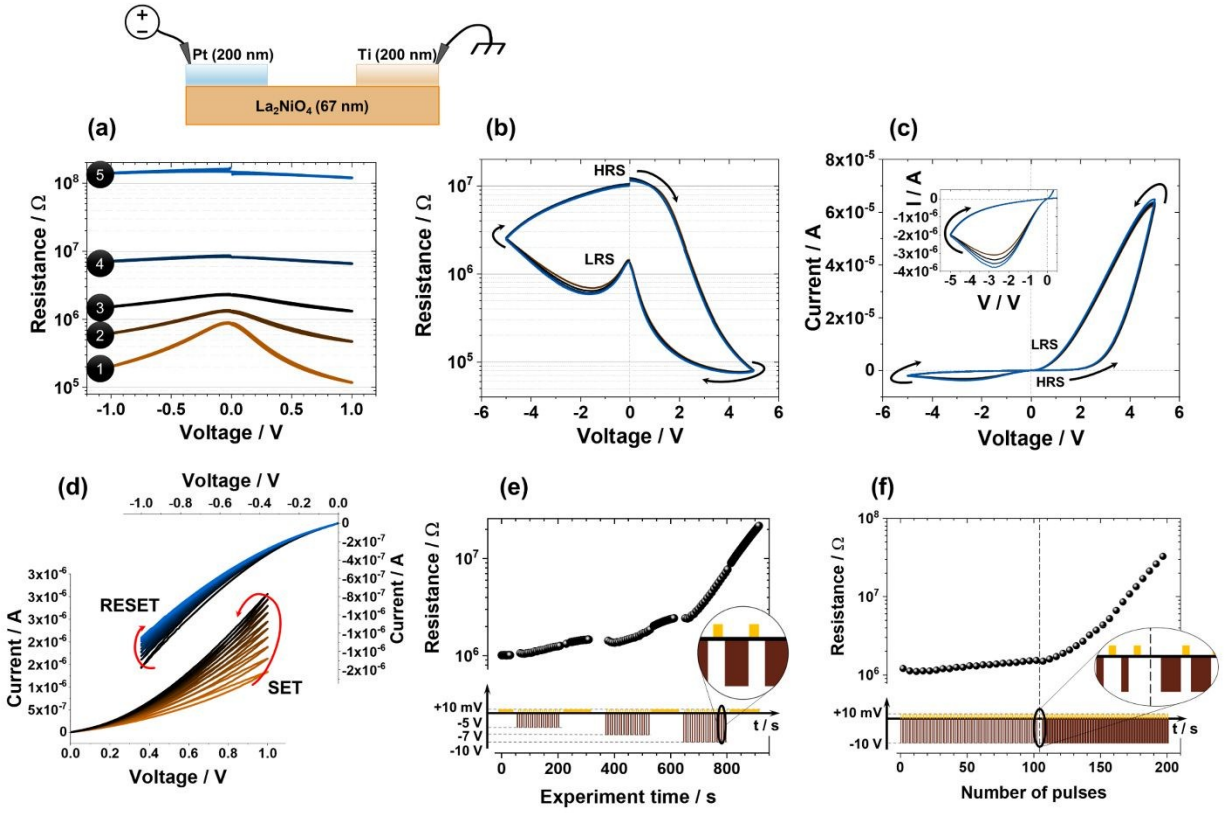

Figure 2: Pt/L2NO4/Ti memristive device (a) Evolution of the R-V characteristics (±1 V, log scale) of a at different stages of the biasing experiment, consisting in the application of increasingly negative voltage pulses as indicated by the numerals (1 = IRS, 2 = 100 s at -1 V, -2 V and -3 V, 3 = 100 s at -4 V, 4 = 100 s at -5 V and 5 = 2x100 s at -5 V). (b,c) Hysteretic R-V and I-V characteristics. The device starts at 0 V in the HRS, is set in its LRS applying a positive bias of +5 V and reset to HRS by applying a negative bias of -5 V. (d) Progressive SET and RESET achieved by carrying out unipolar +1 V and -1 V sweeps, respectively. Resistance vs time measured for (e) 3 trains of 20 pulses (pulse width of 3000 ms) with increasing pulse amplitude (-5 V, -7 V and -10 V) applied to a pristine Pt/L2NO4/Ti device, and (f) 2 trains of 100 pulses of -10 V with increasing pulse width (300 ms and 1500 ms). Only the readouts at +10 mV are shown. The structure of the device is shown schematically on top of the figure.

Journal of Materials Chemistry C
View Article Online
DOI: 10.1039/C9TC03972D

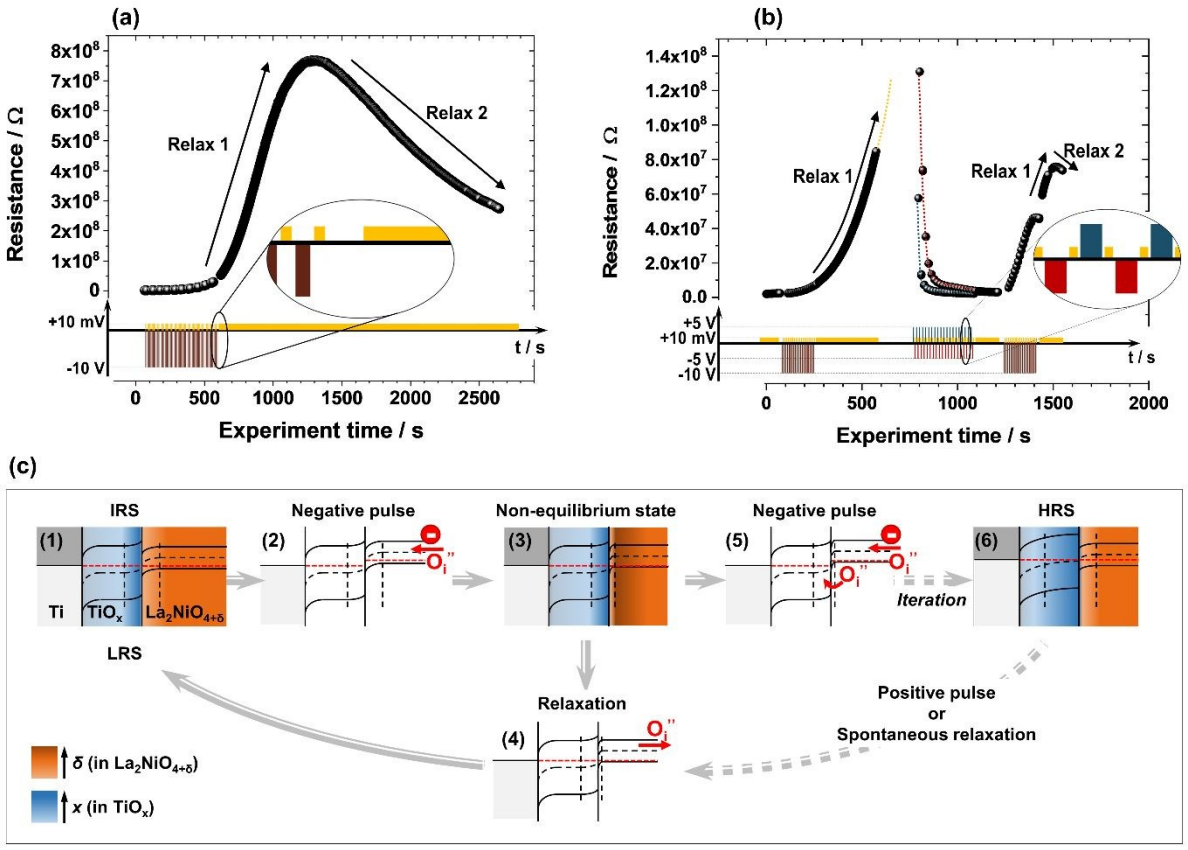

Figure 3: Pt/L2NO4/Ti memristive device (a) Dynamic resistance relaxation measured after programming it to a HRS by applying 100 pulses [-10 V; 1500 ms]. The resistance continues increasing (spontaneously) during the first 720 s before decreasing again to LRS. (b) Evolution of the resistance over time showing the highly multilevel programming capabilities. Only the readouts at +10 mV are represented, (the dotted yellow line is an extrapolation). The dotted red and blue lines correspond to programmed (±5 V) sections of the curve. (c) Schematic illustrations depicting the band-diagram and proposed mechanisms for the interface-type resistance-change in a Pt/L2NO4/Ti device (only the active Ti/TiO_x/L2NO4 junction is represented). The oxygen concentration gradients in TiO_x and L2NO4 are represented by the blue and orange color gradients, respectively. The darker the contrast, the higher the oxygen concentration. See main text for more details about the model.

Journal of Materials Chemistry C
View Article Online
DOI: 10.1039/C9TC03972D

Using a mixed ionic electronic conductor to build an analog memristive device with neuromorphic programming capabilities

Klaasjan Maas, Edouard Villepreux, David Cooper, Carmen Jimenez, Hervé Roussel, Laetitia Rapenne, Xavier Mescot, Quentin Rafhay, Michel Boudard, Mónica Burriel*

Table of Contents:

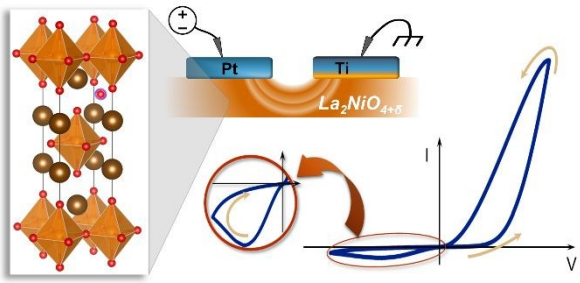

The mixed ionic-electronic conductor $La_2NiO_{4+\delta}$ is used to build interface-type valence-change memories showing transient, multilevel and analog-type memristive properties.